

Ram pressure stripping of the cool core of the Ophiuchus Cluster

E. T. Million,¹ S. W. Allen,¹ N. Werner¹ and G. B. Taylor²

¹*Kavli Institute for Particle Astrophysics and Cosmology, Stanford University, 382 Via Pueblo Mall, Stanford, CA 94305-4060, USA; SLAC National Accelerator Laboratory, 2575 Sand Hill Road, Menlo Park, CA 94025, USA*

²*Department of Physics and Astronomy, University of New Mexico, Albuquerque NM, 87131, USA*

25 October 2018

ABSTRACT

We report results from a *Chandra* study of the central regions of the nearby, X-ray bright, Ophiuchus Cluster ($z = 0.03$), the second-brightest cluster in the sky. Our study reveals a dramatic, close-up view of the stripping and potential destruction of a cool core within a rich cluster. The X-ray emission from the Ophiuchus Cluster core exhibits a comet-like morphology extending to the north, driven by merging activity, indicative of ram-pressure stripping caused by rapid motion through the ambient cluster gas. A cold front at the southern edge implies a velocity of $1000 \pm 200 \text{ km s}^{-1}$ ($M \sim 0.6$). The X-ray emission from the cluster core is sharply peaked. As previously noted, the peak is offset by 4 arcsec ($\sim 2 \text{ kpc}$) from the optical center of the associated cD galaxy, indicating that ram pressure has slowed the core, allowing the relatively collisionless stars and dark matter to carry on ahead. The cluster exhibits the strongest central temperature gradient of any massive cluster observed to date: the temperature rises from 0.7 keV within 1 kpc of the brightness peak, to 10 keV by 30 kpc. A strong metallicity gradient is also observed within the same region. This supports a picture in which the outer parts of the cool core have been stripped by ram-pressure due to its rapid motion. The cooling time of the innermost gas is very short, $\sim 5 \times 10^7$ yrs. Within the central 10 kpc radius, multiple small-scale fronts and a complex thermodynamic structure are observed, indicating significant motions. These may be excited by the separation of the X-ray peak from the cD galaxy and its associated dark matter potential. Beyond the central 50 kpc, and out to a radius $\sim 150 \text{ kpc}$, the cluster appears relatively isothermal and has near constant metallicity. The exception is a large, coherent ridge of enhanced metallicity observed to trail the cool core, and which is likely to have been stripped from it.

Key words: X-rays: galaxies: clusters – galaxies: clusters: individual: Ophiuchus – radiation mechanisms: non-thermal – intergalactic medium

1 INTRODUCTION

The Ophiuchus Cluster ($z = 0.03$) is the second-brightest cluster of galaxies in the 2 – 10 keV sky (Edge *et al.* 1990; see also Ebeling *et al.* 2002). This extremely massive, nearby system lies behind the plane of our Galaxy and is highly obscured, with a line-of-sight equivalent hydrogen column density $N_H \sim 3 \times 10^{21} \text{ atom cm}^{-2}$. Using data from the Einstein Observatory and EXOSAT, Arnaud *et al.* (1987) showed that the cluster has a high mean temperature, $kT = 9.4_{-1.2}^{+1.5}$ keV (90 per cent confidence errors) and hosts a sharply-peaked cooling core. These findings were confirmed by later studies with ASCA (Matsuzawa *et al.* 1996, Watanabe *et al.* 2001) and *Chandra* (Sun *et al.* 2007). Relatively cool, X-ray bright spectral components are associated with the cluster

center, with a minimum measured temperature below 1 keV (Pérez-Torres *et al.* 2009). The peak of the X-ray emission from the cluster is also offset from the X-ray centroid at larger scales (Arnaud *et al.* 1987).

Ascasibar & Markevitch (2006) noted the presence of three surface brightness discontinuities in the central regions of the Ophiuchus Cluster (see also Fig. 1), suggesting significant motion of the cool, dense core. Such fronts are common in clusters and are typically caused by merger events (*e.g.* Vikhlinin, Markevitch & Murray 2001; Reiprich *et al.* 2001). However, many relatively relaxed clusters, such as Abell 1795 and 2029 (Fabian *et al.* 2001; Markevitch, Vikhlinin & Mazzotta 2001; Clarke *et al.* 2004), also exhibit surface brightness discontinuities near their X-ray surface

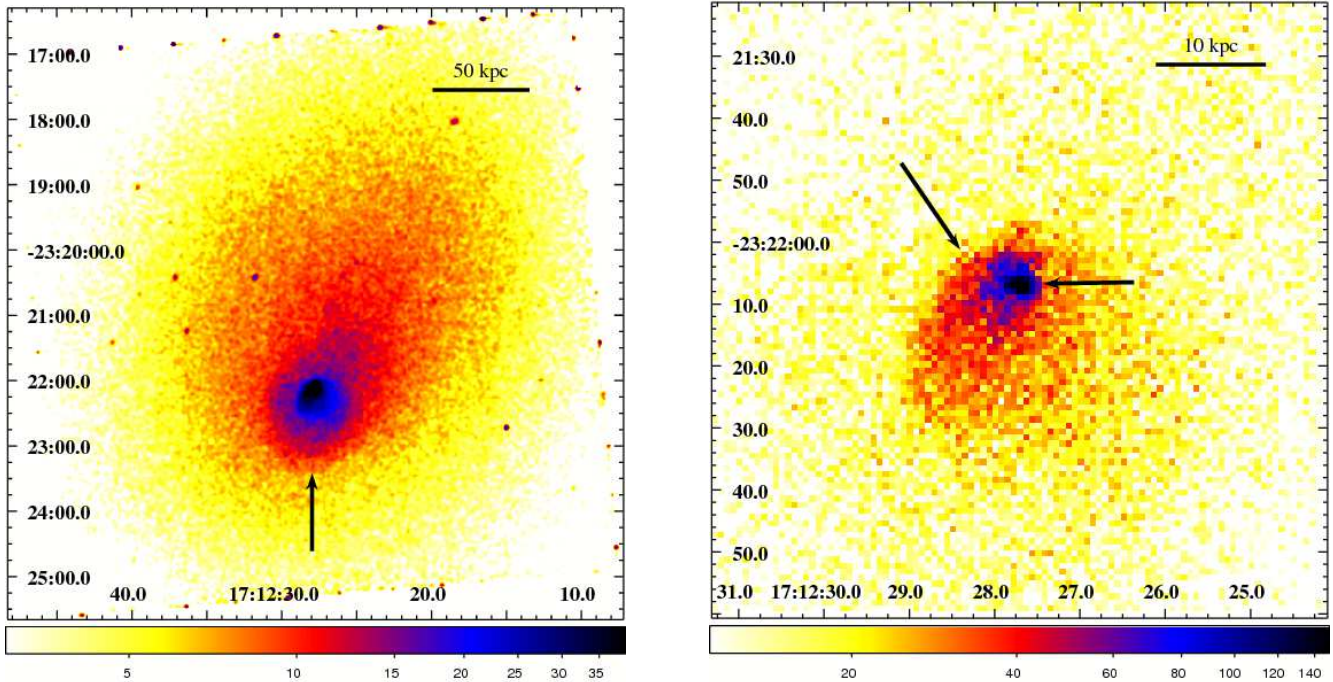


Figure 1. Background subtracted, flat-fielded X-ray surface brightness maps in the 0.6 – 7.0 keV band, smoothed with a 2 arcsec Gaussian filter. The three surface brightness discontinuities noted by Ascasibar & Markevitch (2006) are marked with arrows. (a) The central 8×8 arcmin² region covered by ACIS chip 7. Note the comet-like extension to the north/northwest and the cold front observed ~ 40 kpc to the south of the X-ray peak (see also Ascasibar & Markevitch 2006). (b) The central 1.6×1.6 arcmin² region of the cluster. Two additional surface brightness discontinuities are observed. One is 10 arcsec (5.5 kpc) to the northeast of the X-ray peak, the other is 3 arcsec (1.5 kpc) to the west (see also Ascasibar & Markevitch 2006).

brightness peaks. Simulations suggest that ‘sloshing’ of the gas even in cool core clusters can lead to visible fronts up to several Gyrs after a relatively minor merger event (see Tittley & Henriksen 2005; Ascasibar & Markevitch 2006; see also Markevitch & Vikhlinin 2007 and references within). A cool core in motion within the ambient ICM will also experience ram pressure. The impact of this ram pressure is of particular interest for the survivability of cool cores following major mergers.

Due to its location and large angular size, optical studies of the Ophiuchus Cluster have proved challenging. However, detailed spectroscopic studies suggest that the system is very massive, with a velocity dispersion $\sigma_v = 1050 \pm 50$ km s⁻¹ (Wakamatsu et al. 2005), consistent with the measured X-ray temperature and luminosity (Edge et al. 1990). Clear substructure in the galaxy velocity histogram is observed, indicating that the cluster is merging (Wakamatsu et al. 2005). The dominant cluster galaxy exhibits a substantial peculiar velocity, $v_p = -650$ km s⁻¹, with respect to the cluster mean, $cz = 9045 \pm 30$ km s⁻¹ (Wakamatsu et al. 2005; Hasegawa et al. 2000). The presence of many nearby, smaller clusters and groups argues that Ophiuchus lies at the center of a supercluster (Wakamatsu et al. 2005; see also Hasegawa et al. 2000).

Govoni et al. (2009; see also Murgia et al. 2009) report the discovery of a low surface brightness, diffuse radio mini-halo surrounding the dominant cluster galaxy, 2MASX J17122774-2322108. The central cD galaxy is also detected at 1.4 GHz with a flux density of 29.3 mJy in the NVSS survey (Condon et al. 1998; see also Section 3.1) with

a 45×45 arcsec² (FWHM) synthesized beam. There are a few other strong radio sources at the periphery of the cluster (see Johnston et al. 1981). However, their association with the Ophiuchus Cluster is uncertain. A variety of authors have searched for non-thermal X-ray emission from the cluster in the hard X-ray band (see Nevalainen et al. 2004, 2009; Eckert et al. 2008; see also Dunn & Fabian 2006), although the results to date remain inconclusive (see Fujita et al. 2008; Ajello et al. 2009).

In this paper, we report detailed *Chandra* observations of the core of Ophiuchus Cluster. Section 2 discusses the data reduction and analysis method. Section 3 describes the main results and Section 4 provides physical interpretation. At a redshift of $z = 0.03$, one arcsec corresponds to 0.60 kpc, assuming a Λ CDM cosmology of $H_0 = 70$ km s⁻¹ Mpc⁻¹, $\Omega_M = 0.3$, and $\Omega_\Lambda = 0.7$.

2 OBSERVATIONS AND ANALYSIS

2.1 X-ray data reduction

The *Chandra* observation of the Ophiuchus Cluster (observation ID 3200) was carried out using the Advanced CCD Imaging Spectrometer (ACIS) in October 2002. The standard level-1 event lists produced by the *Chandra* pipeline were reprocessed using the *CIAO* (version 4.1.2) software package, including the appropriate gain maps and calibration products (*CALDB* version 4.1.3). Bad pixels were removed and standard grade selections applied. The data were cleaned to remove periods of anomalously high background,

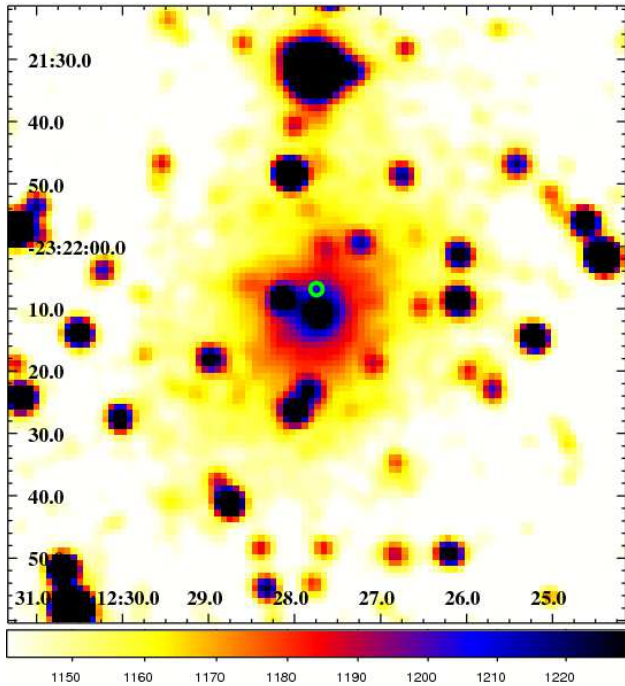


Figure 2. Co-added H, J, and K band 2MASS image of the inner regions of the Ophiuchus Cluster, showing the same region as Fig. 1b. The green circle marks the position of the X-ray brightness peak. The radius of the circle (1 arcsec) represents a conservative estimate of the astrometric uncertainties. As reported by Pérez-Torres *et al.* (2009), the X-ray peak is offset by ~ 2 kpc (4 arcsec) to the north of the central galaxy.

using the standard energy ranges and binning methods recommended by the *Chandra* X-ray Center. The resulting net, clean exposure time is 49.5 ks. Separate photon-weighted response matrices and effective area files were constructed for each region analyzed.

2.2 Spatially-resolved X-ray spectroscopy

2.2.1 Spatial binning

The individual regions for the spectral analysis were determined using the contour binning method of Sanders (2006), which groups neighboring pixels of similar surface brightness until a desired signal-to-noise threshold is met. For data of the quality discussed here, the regions are small enough that the X-ray emission from each can be approximated usefully by a single temperature plasma model. We have focused our analysis on data from the central back-illuminated ACIS-S chip (chip 7).

We initially carried out thermodynamic mapping with $\sim 10,000$ net counts per region, to examine the thermodynamic structure of the hottest gas in the cluster on large scales. This allows us to measure the metallicity and temperature of gas with $kT \sim 10$ keV to an accuracy of ~ 10 per cent. Higher-resolution thermodynamic mapping of the central 40 kpc was also performed, with $\sim 3,000$ net counts per region, to examine the thermodynamic structure of the cooler cluster core. This allows us to measure the metallicity of this gas to better than 20 per cent, and the temperature of regions with $kT < 5$ keV to ~ 5 per cent accuracy or better.

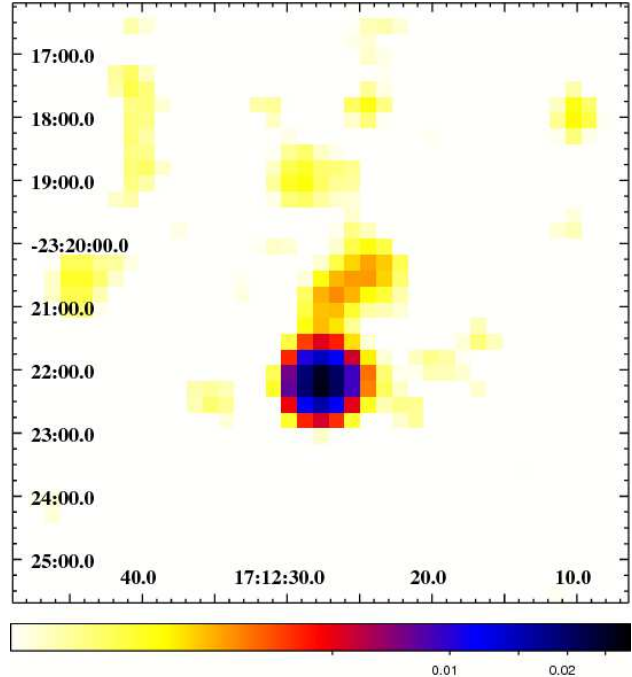


Figure 3. 1.4 GHz NVSS image (Condon *et al.* 1998) of the Ophiuchus Cluster spanning the same region as figure 1a. A bright central radio source is coincident with the location of the central galaxy. The spatial resolution of the radio data is approximately 45×45 arcsec² (FWHM; see also Pérez-Torres *et al.* 2009). The radio emission extends to the northwest, similar to the comet-like X-ray morphology.

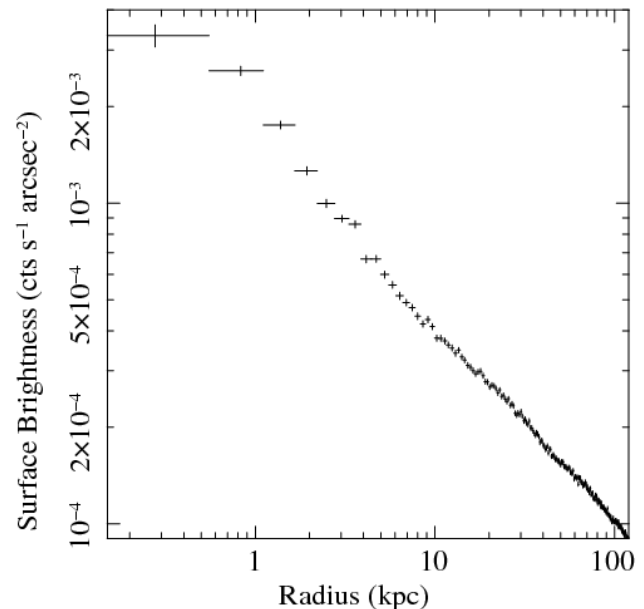


Figure 4. Azimuthally-averaged surface brightness profile in the 0.6 – 7.0 keV band, centered on the X-ray peak. The profile is very sharp and no clear central flattening is observed.

In order to determine radial profiles for thermodynamic properties, we have also extracted spectra in concentric circular annuli, centered on the X-ray peak position. The widths of the annuli range from 1 arcsec to 40 arcsec.

2.2.2 Background modelling

Background spectra for the appropriate detector regions were extracted from the blank-sky fields available from the *Chandra* X-ray Center. The blank-sky fields were processed in an identical manner to the Ophiuchus Cluster observation, and were reprojected onto the same coordinates using the appropriate aspect solution files. Background regions were chosen to match the same extraction regions as the science data. The background spectra were normalized by the ratio of the observed and blank-sky count rates in the 9.5 – 12 keV band (due to the very small effective area of the *Chandra* telescope at hard X-ray energies, there is no significant cluster emission in the 9.5 – 12 keV band). The statistical uncertainty in the observed 9.5 – 12 keV flux is less than 5 per cent.

To enable further refinement of the background models, we have also extracted spectra from relatively source-free regions of the other back-illuminated ACIS CCD (chip 5). Although cluster emission is still clearly present on this offset chip, it is significantly fainter than on the central chip (Chip 7) and the data from it can be compared to the blank-sky fields to identify any additional, strong foreground/background emission components. Such components are commonly detected in the spectra of sources lying behind the Galactic Plane. We indeed detect excess soft emission with respect to the blank sky fields in the Ophiuchus data, which is modelled in the analysis. We note, however, that our results on the bright cluster core are relatively insensitive to the details of the background modelling.

2.2.3 Spectral analysis

The spectra have been analyzed using XSPEC (version 12.5; Arnaud 1996), the MEKAL plasma emission code (Kaastra & Mewe 1993), and the photoelectric absorption models of Balucinska-Church & McCammon (1992). All spectral fits were carried out in the 0.6 – 7.0 keV energy band. The extended C-statistic available in XSPEC was used for all fitting.

The default spectral model applied to each spatial region consists of an optically-thin, MEKAL thermal plasma model, at the redshift of the cluster. The normalization, temperature, and metallicity¹ in each spatial region are free parameters in the fits. Since the Galactic column density determined from HI studies is high (Kalberla *et al.* 2005; see also Dickey & Lockman 1990), we include this as an additional free parameter in the analysis, linked to vary in unison across all regions. We have also examined models where the column density is allowed to vary spatially.

In Section 3.5, we briefly discuss results from a search for non-thermal X-ray emission from the cluster. In this case, additional power-law model components were included in

the analysis, following the method described by Million & Allen (2009).

For the determination of deprojected radial profiles from the azimuthally-averaged spectra, we use the PROJCT model in XSPEC.

3 RESULTS

3.1 Imaging analysis

Background subtracted, flat-fielded images in the 0.6 – 7.0 keV band were extracted on a 0.984×0.984 arcsec² pixel scale. Fig. 1a shows the X-ray image for the region spanning the central ACIS chip (approximately 8×8 arcmin²). The peak of the X-ray emission lies at coordinates $\alpha(2000) = 17^{\text{h}}12^{\text{m}}27.64^{\text{s}}$, $\delta(2000) = -23^{\circ}22^{\text{m}}07.0^{\text{s}}$. This peak is embedded in an extended X-ray bright halo, which has a comet-like tail extending to the north/northwest. A clear surface brightness discontinuity or ‘cold front’ is observed at a radius of 40 kpc to the south of the X-ray surface brightness peak (first noted by Ascasibar & Markevitch 2006). The overall X-ray morphology suggests that the cluster core is travelling approximately north to south, along a position angle of ~ 160 degrees, with ram-pressure leading to the formation of the comet-like tail behind it.

Fig. 1b shows the central 1.6×1.6 arcmin² region of the cluster. Two additional sharp surface brightness fronts (also noted by Ascasibar & Markevitch 2006), are observed at radii of ~ 3 and ~ 10 arcsec to the west and northeast of the X-ray peak, respectively. These fronts appear to be sites of significant shearing and suggest significant swirling and sloshing within the inner, X-ray bright cluster core.

Fig. 2 shows the co-added H, J, K band 2MASS image for the same, central 1.6×1.6 arcmin² region. The dominant cluster galaxy is seen near the center of the field. The green circle in the figure marks the location of the X-ray peak; the radius of the circle provides a conservative estimate of the astrometric uncertainty in the X-ray astrometry (~ 1 arcsec). As was also reported by Pérez-Torres *et al.* (2009), the optical centroid is offset to the south of the X-ray peak by 4 arcsec (2 kpc). This offset presumably reflects the impact of ram pressure in slowing down the X-ray emitting gas, and the essentially collisionless nature of the stars (and dark matter) associated with the galaxy, which carry on ahead.

Fig. 3 shows the 1.4 GHz NVSS image (Condon *et al.* 1998; the resolution is approximately 45×45 arcsec²; FWHM) for the same field of view as Fig. 1a. A bright, central radio source is observed at a position approximately coincident with the position of the central galaxy. A low surface brightness radio feature extends towards the northwest, much like the comet-like trail in X-rays, although the signal-to-noise ratio is low. Higher-resolution and deeper multi-frequency radio data are required to determine the origin of this feature as well as the detailed relation to the complex central X-ray emission.

The X-ray surface brightness profile for the cluster about the X-ray peak is shown in Fig. 4. The profile is very sharp and no clear central flattening is observed. The profile can be approximated by a power law model, $S_0 R^{-\alpha}$, with slope $\alpha = 0.6112 \pm 0.0015$, or a β model with $\beta = 0.2685 \pm 0.0002$ and core radius $r_c < 0.5$ kpc. However, nei-

¹ Cluster abundances are calculated with respect to Anders & Grevesse (1989).

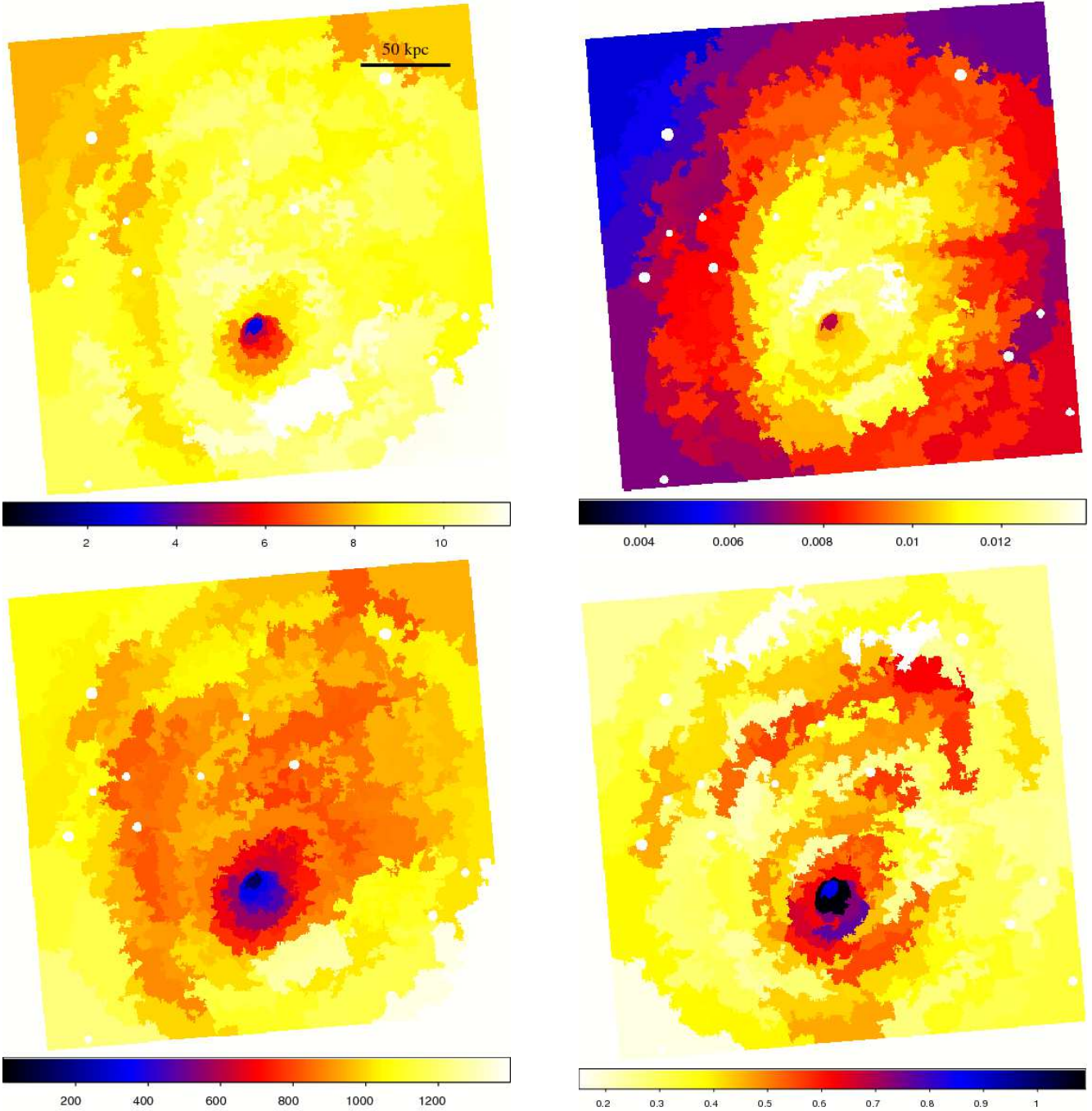


Figure 5. Temperature map (upper left; in keV), pressure map (upper right; in $\text{keV cm}^{-5/2} \text{arcsec}^{-1}$), entropy map (lower left; in $\text{keV cm}^{5/3} \text{arcsec}^{2/3}$), and metallicity map (lower right; in solar) for the field of view covered by ACIS Chip 7 (see Fig. 1a). Individual regions follow lines of constant surface brightness, while maintaining a constant signal to noise threshold ($\sim 10,000$ net counts per region). This results in statistical uncertainties on the temperature and metallicity of ~ 10 per cent or better. The electron number density is approximated as $\sqrt{K/A}$, where K is the MEKAL normalization and A is the projected area.

ther simple model provides a formally acceptable fit to the data.

3.2 Thermodynamic mapping

3.2.1 Large scale properties

Fig. 5 shows the large scale thermodynamic structure of the cluster, on the same spatial scale as Fig. 1a. From top to bottom, left to right, we show temperature, pressure, entropy and metallicity maps. These quantities show significant mor-

phological correspondence with the X-ray surface brightness image. The X-ray bright core contains relatively cool, low entropy gas. This gas has a high metallicity. Beyond the central 30 kpc radius, the temperature map is relatively isothermal.

Beyond the inner 30 kpc region, no clear gradients in metallicity are observed. However, a large, metal-rich ridge spans position angles of -50 to 45 degree, at a radius of ~ 100 kpc to the north of the cluster core. This ridge consists of 5 independent, coherent, metal rich regions. The mean metallicity of the 5 regions is 0.55 ± 0.04 solar, which is approximately 1.8 times greater than the mean value of 0.30 ± 0.03 solar determined for the 9 adjacent regions. A second ridge of enhanced metallicity appears to partially encircle the cluster core at a radius of ~ 40 kpc spanning position angles of -55 to 270 degrees at a radius ~ 40 kpc. To the south, where the metallicity of the ridge is highest, it is approximately coincident with the location of the southern cold front. This southern ring-like ridge contains 10 coherent, independent regions of measured high metallicity. The mean metallicity of these 10 regions is 0.51 ± 0.04 solar, which is approximately 1.5 times greater than the mean value of 0.34 ± 0.04 solar determined from the 7 adjacent regions at larger radius.

In the above analysis, the absorption was linked to vary in unison across all regions. We have also investigated other absorption models.² When allowing the absorption to be independently free in each region, we obtain the map shown in Fig. 6. A trend towards higher absorption is observed in the cluster center, similar to Abell 478 (Allen *et al.* 1993; Sun *et al.* 2003). The innermost bin exhibits somewhat lower apparent absorption, although this may be an artifact due to the complex thermal structure of the X-ray emission from this region. A coherent structure of excess absorption appears to cross through the cluster, with the western side of the field being more absorbed than the east.

3.2.2 Properties of the inner cluster core

Fig. 7 shows the temperature, pressure, entropy and metallicity maps for the inner ~ 40 kpc radius region. The maps reveal steeply declining temperature and entropy as one moves inward toward the X-ray peak. The morphology of the lowest temperature gas traces a swirl structure also seen in the surface brightness map (Fig 1b). Interestingly, the X-ray brightness peak does not coincide with the pressure maximum: the latter is located to the north of the brightness peak, and trails the inferred southward motion.

The central region of the cluster shows an enormous range of temperature, from less than 1 keV to greater than 10 keV. This is only the second hot, massive cluster to show sub 1.0 keV gas in spectral maps (see also the study of Abell 2204 by Sanders *et al.* 2009). If the cluster were at significantly higher redshift, this coolest gas would not be spatially resolved.

² The qualitative structures of the thermodynamic maps are unchanged using different absorption models. We note, however, that the exact value of the temperature and quantities derived thereof vary by up to 10 per cent, depending on the exact value of the column density.

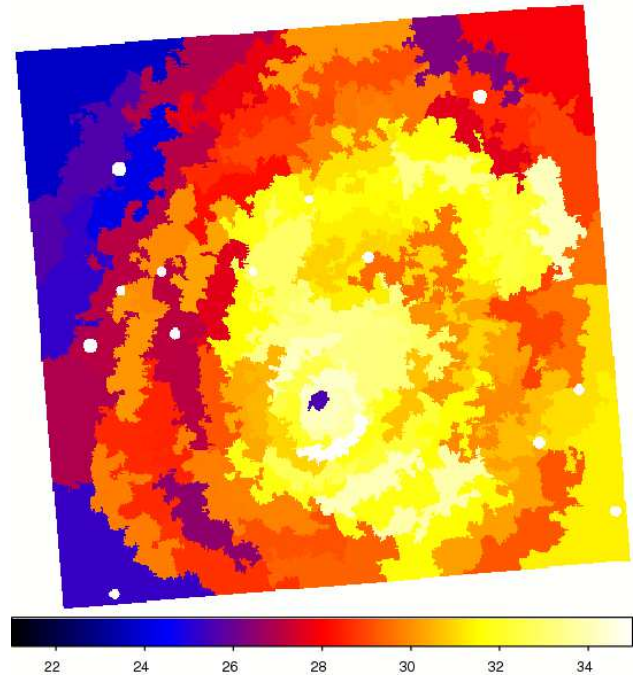


Figure 6. Map of the measured equivalent, line-of-sight absorbing hydrogen column density (in units of 10^{20} atom cm^{-2}) for the region covered by ACIS chip 7 (same region as Fig. 1a). Other details as for Fig. 5. The statistical uncertainties in the measurements are at the ~ 5 per cent level.

3.3 Azimuthally-averaged, radial profiles

Fig. 8 shows the azimuthally-averaged, projected temperature and metallicity profiles for the cluster, centered on the X-ray peak. The profiles reveal a steep central temperature gradient within the central 30 kpc radius. Beyond $r \sim 50$ kpc, the cluster appears remarkably isothermal. The same central 30 kpc also exhibits a complex metallicity profile, which first rises steeply with increasing radius, from 0.1 solar within 0.5 kpc to almost twice solar at 3–5 kpc. Between $5 < r < 50$ kpc, the metallicity declines steadily before becoming approximately constant for $r \gtrsim 50$ kpc, out to the edge of the field.

Fig. 9 shows the deprojected temperature, density, pressure, entropy, cooling time and metallicity profiles, determined under the assumption of spherical symmetry. We caution that departures from spherical symmetry will have some effect on the electron density, pressure, entropy, and cooling time profiles. The deprojected profiles confirm the presence of a strong, central temperature gradient, which rises with increasing radius by over a factor of 10 within the central 30 kpc. The minimum temperature, measured within the central 1 kpc, is ~ 0.7 keV, consistent with that of large, elliptical galaxies. Indeed, it may be that this coolest gas was originally the interstellar medium of the dominant cluster galaxy, which has been stripped by ram pressure. By 30 kpc, the temperature has risen to 10 keV. This is the strongest central temperature gradient observed in any cluster to date.

The central cooling time is very short, dropping below 4×10^7 yrs. The central metallicity gradient is even more pronounced in the deprojected profiles, with $Z \sim 0.25$ solar within 1 kpc, a peak at $Z \sim 3$ solar at $r \sim 5$ kpc, and

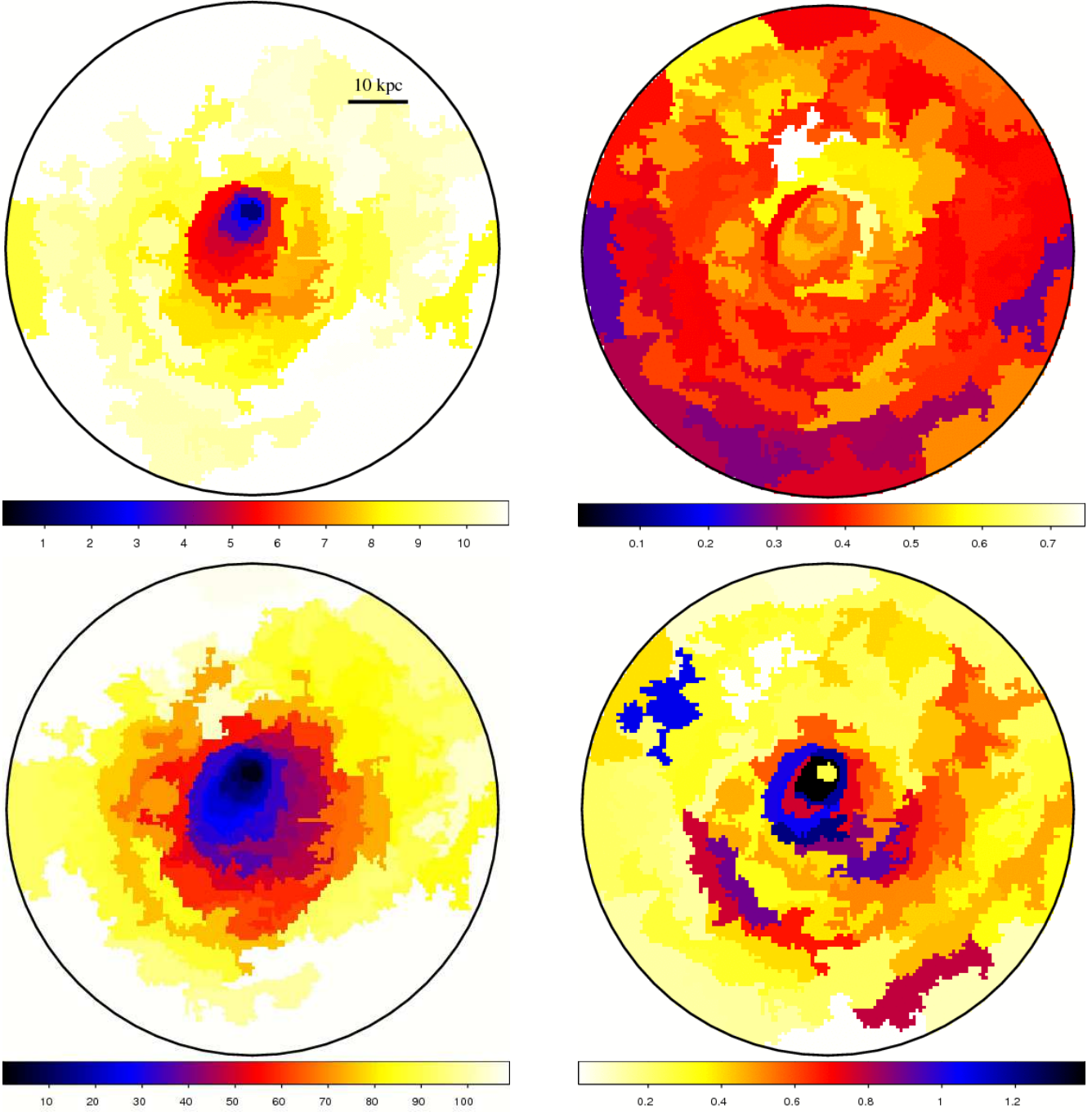


Figure 7. Temperature (upper left, in keV), pressure (upper right, in keV cm^{-3}), entropy (lower left, in keV cm^2), and metallicity (lower right, solar) maps for the central ~ 40 kpc radius of the Ophiuchus Cluster. Regions maintain a constant signal to noise threshold ($\sim 3,000$ net counts per region), resulting in statistical uncertainties of ~ 5 per cent in temperature, for $kT < 5$ keV. Here, we approximate the volume of each emission region as $\frac{2}{3}Al$, where A is the projected area and l is the line of sight distance; $l = \sqrt{r_{max}^2 - r_{min}^2} \cdot r_{max}$ and r_{min} are the maximum and minimum distances for all points in a region, from the X-ray surface brightness peak (see Henry *et al.* 2004, Mahdavi *et al.* 2005). The number density is calculated from the MEKAL normalization.

dropping again at larger radii. We caution, however, that the low central metallicity may in part be an artifact due to complex temperature structure in the innermost regions (see Werner *et al.* 2008 and references within). Beyond $r \sim 50$ kpc, the temperature and metallicity remain approximately constant at $kT \sim 10$ keV and $Z \sim 0.35$ solar, respectively, to the edge of the field of view.

Within 5 kpc of the X-ray peak, the deprojected pressure profile declines. The maximum pressure is observed 5 kpc from the center. Our thermodynamic maps (Fig. 7b) show that the pressure peak lies to the north of the brightness peak. Extrapolating the pressure profile for $r > 5$ kpc inward to the core, we estimate that the innermost regions are under-pressured by ~ 60 per cent. This argues

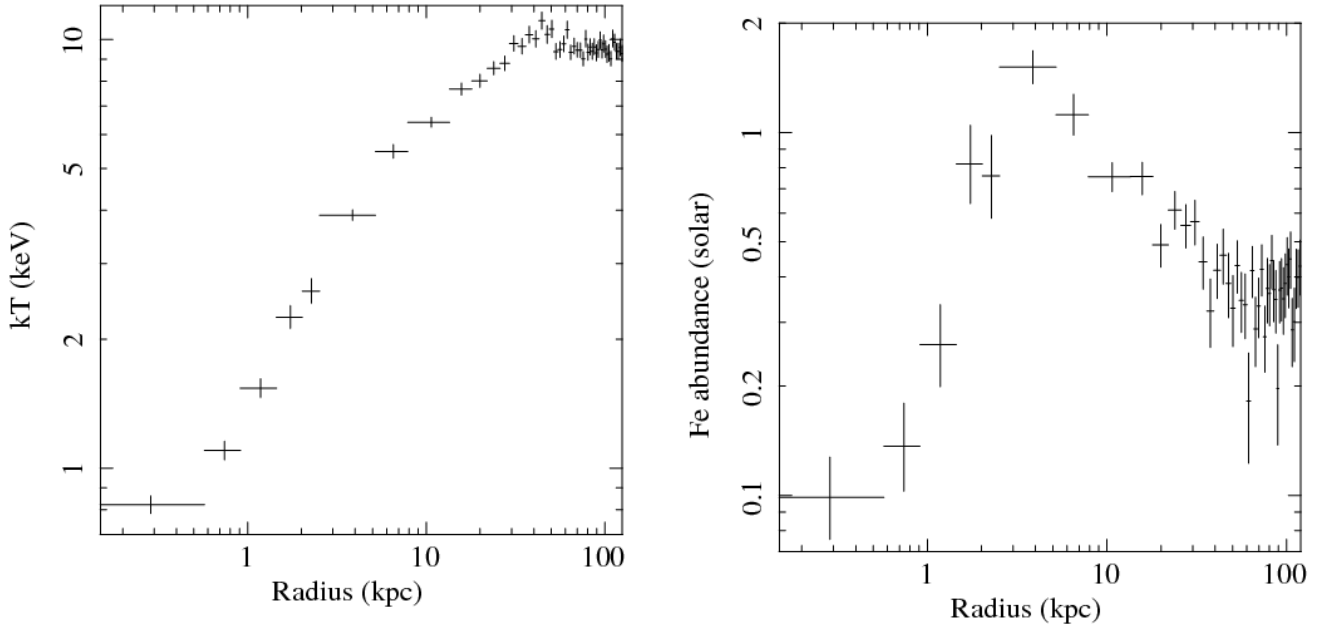


Figure 8. Azimuthally-averaged, projected temperature (left; in keV) and Fe abundance (right; in solar units) profiles, centered on the X-ray peak. The temperature profile shows a strong central gradient within 30 kpc. The central abundance is low, rises to a maximum value $Z = 1.5^{+0.17}_{-0.15}$ by 5 kpc, before declining again to a value $Z \sim 0.35$ at 30 kpc. For radii $r > 50$ kpc, the projected temperature and metallicity remain approximately constant.

for substantial non-thermal pressure support in these regions, which is probably dominated by gas motions, as suggested by the multiple brightness fronts and X-ray-optical displacement seen in Fig. 2. Turbulent motions at the level of $\sim 500 \text{ km s}^{-1}$ could in principle explain the thermal pressure deficit. However, it is also possible that non-thermal particles contribute to the total pressure support in the core. Higher resolution radio data are required to explore this possibility.

3.4 Analysis of the southern cold front

A cool, dense core moving through a diffuse hot, gaseous halo will experience ram pressure. In detail, the pressure ratio at the cold front leading the core is related to the core velocity by (Landau & Lifshitz 1959; see also Vikhlinin *et al.* 2001)

$$\frac{p_0}{p_1} = \left(1 + \frac{\gamma - 1}{2} M^2\right)^{\frac{\gamma}{\gamma - 1}}, M \leq 1 \quad (1)$$

$$\frac{p_0}{p_1} = \left(\frac{\gamma + 1}{2}\right)^{\frac{\gamma + 1}{\gamma - 1}} M^2 \left[\gamma - \frac{\gamma - 1}{2M^2}\right]^{\frac{-1}{\gamma - 1}}, M > 1, \quad (2)$$

where $M = v/c$ is the Mach number of the core through the hot diffuse gas, and $\gamma = 5/3$ is the adiabatic index. Here, index 1 refers to the ambient, hot gas and index 0 to the moving, cool core.

We have applied these calculations to the southern cold front at $r \sim 40$ kpc, which has a relatively simple geometry and appears to lead the overall motion of the cool core. For this analysis we examine the deprojected pressure profile in a 110 degree slice, centered on the center of curvature of the front. Accounting for the underlying ambient pressure profile, measured in other directions, we determine a pressure ratio at the southern cold front of $p_0/p_1 = 1.3 \pm 0.2$. This

corresponds to a Mach number of 0.58 ± 0.10 and, for an ambient temperature $kT = 10.6 \pm 0.3$ keV, implies a velocity of $1000 \pm 200 \text{ km s}^{-1}$.

The significant rotational motions that appear to be associated with the two other fronts discussed in Section 3.1 prevent any reliable quantitative determinations of their velocities.

3.5 A search for possible non-thermal-like emission

Recently, a detection of a non-thermal X-ray emission component from the Ophiuchus Cluster was claimed by Eckert *et al.* (2008) using data from the *INTEGRAL* satellite. These results are in apparent tension with those from *Suzaku* and *Swift/BAT* (see Fujita *et al.* 2008; Ajello *et al.* 2009).³ In general, proper temperature modelling is crucial in determining the presence, or otherwise, of non-thermal spectral components in the X-ray band. As shown in Fig. 8, a steep temperature profile exists in the central 30 kpc (~ 1 arcmin) of the cluster and must be accounted for. Residual calibration uncertainties will also affect the measured temperature and the inferred non-thermal emission properties. For example, a change in the globally-averaged temperature of ~ 1 keV, for a $kT \sim 10$ keV system like the Ophiuchus Cluster, can change the expected thermal flux above 20 keV by ~ 30 per cent. Such effects currently make it difficult to provide any definite statements on the presence or other-

³ A re-analysis of *INTEGRAL* data, also using *XMM-Newton* data to constrain the thermal emission at lower energies (Nevalainen *et al.* 2009), is consistent with the upper limits obtained by Fujita *et al.* (2008) and Ajello *et al.* (2009).

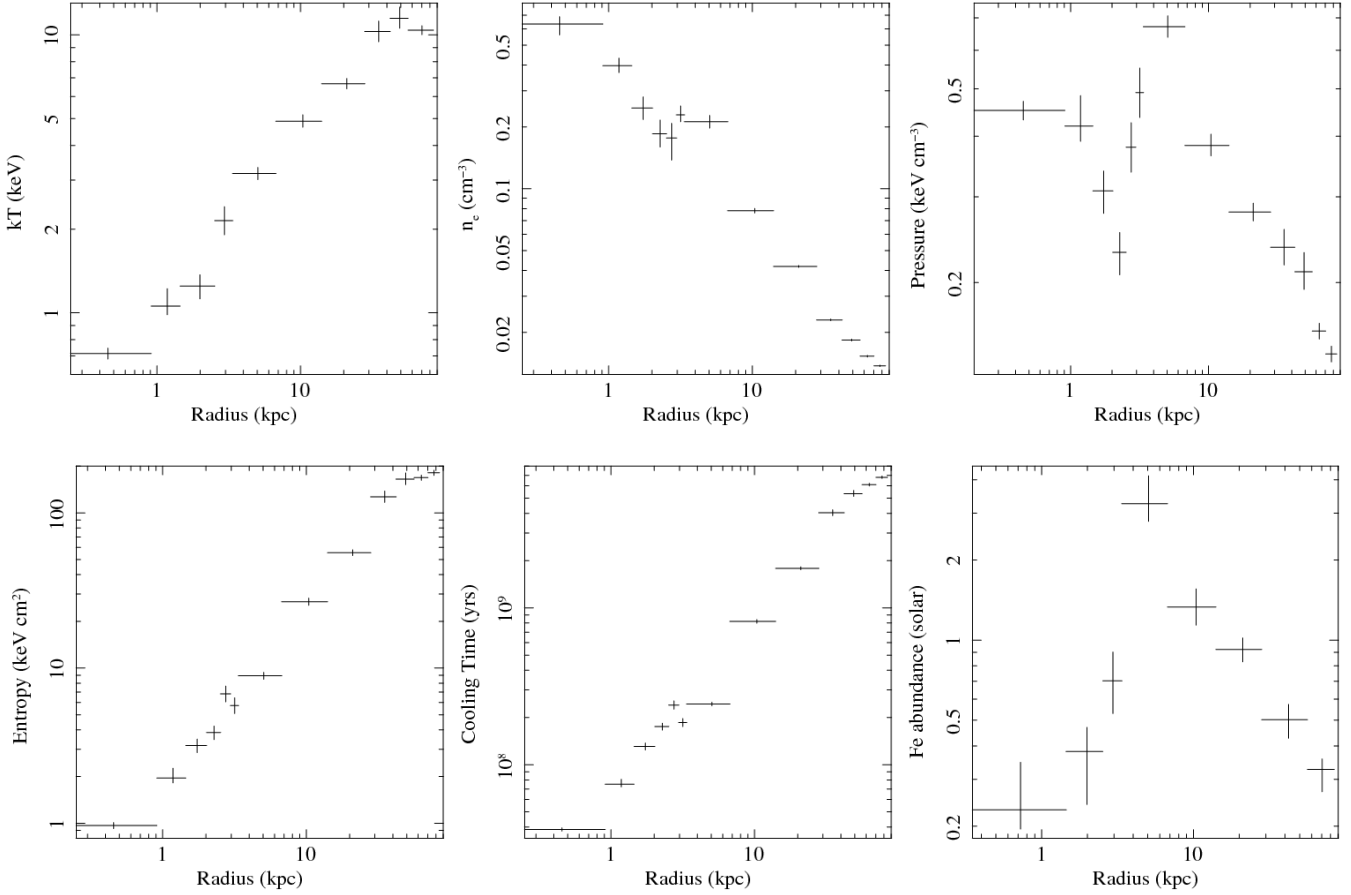


Figure 9. Deprojected temperature (upper left; in keV), electron density (upper middle; in cm^{-3}), pressure (upper right; in keV cm^{-3}), entropy (lower left; keV cm^2), cooling time (lower middle; in years), and Fe abundance (lower right; with respect to solar) profiles. Profiles are centered on the X-ray peak and assume spherical symmetry. Significant asymmetries in the cluster are present, although the results obtained from deprojecting partial angular sectors of the cluster are broadly consistent. We caution that departures from spherical symmetry will have some effect on the electron density, pressure, entropy, and cooling time profiles.

wise of possible non-thermal X-ray spectral components in the Ophiuchus Cluster.

Despite these difficulties, we have searched for non-thermal spectral components in the *Chandra* data following the procedures outlined by Million & Allen (2009). In detail, we have examined the statistical significance of the improvements to the fits that can be obtained with the inclusion of additional power-law components in the spectral modelling. The normalization of the power-law component in each spectral region was a free parameter, while the photon index was fixed to $\Gamma = 2.0$. The statistical signal from all regions was combined to determine the final result on the presence of possible power-law emission.

We find no statistical signal of non-thermal-like components in the *Chandra* data, once the complex, underlying temperature structure revealed by our analysis is taken into account. Allowing the column density in each region to be fit independently, we obtain a 90 per cent confidence upper limit on the flux of any $\Gamma = 2.0$ power-law component from the central 8×8 arcmin² region covered by the ACIS-S chip 7 (excluding only the central 5 kpc region where the temperature drops precipitously and projection effects will be large)

of 2.2×10^{-11} ergs $\text{s}^{-1} \text{cm}^{-2}$ in the 0.6–7.0 keV band.⁴ This upper limit is approximately 10 per cent of the measured total flux in the same region. Our results are consistent with those of Pérez-Torres *et al.* (2009), Ajello *et al.* (2009), and Fujita *et al.* (2008). Our upper limits are at a similar level to the reported detection of non-thermal flux by Nevalainen *et al.* (2009) for the central 7 arcmin radius region. We note that our result depends slightly upon assumptions regarding the Galactic absorption in the direction of the cluster. Fixing the column density for all regions to $N_H = 3 \times 10^{21}$ atom cm^{-2} (the average value determined for all regions), our upper limit is increased to 2.7×10^{-11} ergs $\text{s}^{-1} \text{cm}^{-2}$. Due to observing energy band and field of view differences, direct comparisons with *INTEGRAL* results (Eckert *et al.* 2008) are challenging. Additional hard X-ray data, for example from the forthcoming *NuSTAR* satellite (Harrison *et al.* 2005) are required to rule definitively on this issue.

⁴ Our upper limits are determined from the sums of the power-law normalizations for the 95 regions with each region having an MCMC chain of length 10^4 samples after correcting for burn in.

4 DISCUSSION

The comet-like X-ray morphology, large-scale thermodynamic maps, and clear pressure jump at the location of the southern cold front (Figs. 1a, 5, 7), show that the cool, dense core of the cluster is moving rapidly through the large-scale hot, diffuse cluster medium. The velocity implied by the observed pressure jump at the southern cold front is ~ 1000 km s⁻¹. The peculiar velocity of the cD galaxy of ~ 650 km s⁻¹ with respect to the cluster mean (Wakamatsu *et al.* 2005; Hasegawa *et al.* 2000) also suggests significant, line-of-sight motion. Such speeds may indicate extreme ‘sloshing’ of the cluster core (*e.g.* Markevitch *et al.* 2001; Reiprich *et al.* 2001; Tittley & Henriksen 2005; Ascasibar & Markevitch 2006; see also Markevitch & Vikhlinin 2007 and references within).

The X-ray emission associated with the cool core is very sharply peaked. The coolest ($kT \sim 0.7$ keV), lowest-entropy gas lies within 1 kpc of the brightness peak. This material has a very short cooling time, with $t_{\text{cool}} \sim 4 \times 10^7$ yr, and plausibly represents the stripped interstellar medium of the dominant cluster galaxy.

The high relative velocity of the cool core argues that it was displaced from the base of the cluster potential well, presumably by recent merger activity. This is consistent with the slightly offset location of the X-ray peak with respect to the X-ray centroid at larger scales (Arnaud *et al.* 1987). The case for a recent major merger event is supported by the significant substructure in the galaxy velocity histogram. Given the environment of the present-day cluster, which lies at the center of a supercluster and is surrounded by smaller galaxy groups and clusters, a recent merger event would not be surprising.

The degree to which cool cores are disrupted or destroyed during cluster mergers is an outstanding question in cluster physics, with important implications for cosmological studies (*e.g.* Burns *et al.* 2008; Mantz *et al.* 2009a,b; Ebeling *et al.* 2009). The comet-like morphology of the cool core, and the remarkably steep central temperature gradient (rising from ~ 0.7 keV to 10 keV within a 30 kpc radius) suggest that its outer regions have already been stripped by ram pressure, due to its rapid motion. Our data provide a dramatic, close-up view of the ongoing stripping and potential destruction of a cool core in a rich cluster and have clear implications for the survivability of such cool cores. It will be important to examine, using constrained hydrodynamical simulations, the evolutionary path of such a cool core as it continues to be stripped and its motion slows. At this point it is not clear how much of the original cool core will remain by the time the system returns to equilibrium.

The X-morphology of the inner 10 kpc region (Fig 1b), the separation between the X-ray and optical/near-IR brightness peaks (the X-ray emission trails the cD galaxy) and the offset between the X-ray peak and thermodynamic pressure maximum (the pressure maximum trails the X-ray brightness peak), all suggest additional, significant motions *within* the cool core. The sharp fronts noted in Fig. 1b suggest that significant rotational motion is present, and that the coolest, X-ray brightest gas is moving within the central potential. Such motion is not surprising, given the separation of X-ray peak from the stellar and, presumably, dark

matter potentials of the cD galaxy (Fig. 2).⁵ The sharp fronts seen in Fig 1b are likely to be sites of shearing instabilities, which could lead to rapid mixing of the coolest gas with its surrounding environment.

The ridges of enhanced metallicity in the cluster are particularly interesting. These large-scale, coherent structures are almost twice as metal rich as the surrounding gas. The prominent metallicity ridge 100 kpc to the north of the X-ray peak, and trailing in its wake, appears likely to have been stripped from the cool core during its motion. This ridge, and the partial ring-like ridge of high metallicity material at a radius of ~ 40 kpc, may initially have been driven outward by the central AGN, possibly even during the same outburst. The proximity of this ring to the southern cold front argues that this metal rich gas is currently being stripped from the cool core. A qualitatively similar high-metallicity ridge is also seen in the central regions of the Perseus Cluster (Sanders *et al.* 2005).

Govoni *et al.* (2009) show that the cD galaxy is surrounded by a bright, diffuse mini-halo of synchrotron radio emission. Despite the fact that a significant non-thermal particle population must be present to explain the radio emission, our study provides no evidence for non-thermal X-rays from the central regions of the cluster. High-resolution radio data for the cluster core are not currently available. It will be important to obtain such data and examine the impact of the cluster dynamics on the properties of the central radio source, and the interaction between this source and its surrounding environment.

ACKNOWLEDGMENTS

We thank Anja von der Linden for help with the analysis of the 2MASS data, Glenn Morris for computational support, and Jeremy Sanders for making the contour binning algorithm publicly available. The computational analysis was carried out using the KIPAC XOC compute cluster at Stanford University and the Stanford Linear Accelerator Center (SLAC). Norbert Werner is supported by the National Aeronautics and Space Administration through Einstein Postdoctoral Fellowship Award Number PF8-90056 issued by the Chandra X-ray Observatory Center, which is operated by the Smithsonian Astrophysical Observatory for and on behalf of the National Aeronautics and Space Administration under contract NAS8-03060. This work was supported in part by the U.S. Department of Energy under contract number DE-AC02-76SF00515.

REFERENCES

Ajello M., Rebusco P., Cappelluti N., Reimer O., Böhringer H., Greiner J., Gehrels N., Tueller J., Moretti A., 2009, *ApJ*, 690, 367

⁵ More dramatic offsets between the X-ray emitting gas, and stellar and dark matter mass, have previously been seen in massive, bimodal cluster mergers such as the Bullet Cluster (Clowe *et al.* 2006; Bradac *et al.* 2006) and MACSJ0025.4-1222 (Bradac *et al.* 2008).

- Arnaud K.A., Johnstone R.M., Fabian A.C., Crawford C.S., Nulsen P.E.J., Shafer R.A., Mushotzky R.F., 1987, *MNRAS*, 227, 241
- Arnaud, K.A., 1996, in *Astronomical Data Analysis Software and Systems V*, eds. Jacoby G. and Barnes J., ASP Conf. Series volume 101, p17
- Allen S.W., Fabian A.C., Johnstone R.M., White D.A., Daines S.J., Edge A.C., Stewart G.C., 1993, *MNRAS*, 262, 901
- Anders E., Grevesse N., 1989, *GeCoA*, 53, 197
- Ascasibar Y., Markevitch M., 2006, *ApJ*, 650, 102
- Balucinska-Church M., McCammon D., 1992, *ApJ*, 400, 699
- Bradac M., Clowe D., Gonzalez A.H., Marshall P., Forman W., Jones C., Markevitch M., Randall S., Schrabback T., Zaritsky D., 2006, *ApJ*, 652, 937
- Bradac M., Allen S.W., Treu T., Ebeling H., Massey R., Morris R.G., von der Linden A., Applegate D., 2008, *ApJ*, 687, 959
- Burns J.O., Hallman E.J., Gantner B., Motl P.M., Norman M.L., 2008, *ApJ*, 675, 1125
- Clarke T.E., Blanton E.L., Sarazin C.L., 2004, *ApJ*, 616, 178
- Clowe D., Bradac M., Gonzalez A.H., Markevitch M., Randall S.W., Jones C., Zaritsky D., 2006, *ApJ*, 648L, 109
- Condon J.J., Cotton W.D., Greisen E.W., Yin Q.F., Perley R.A., Taylor G.B., Broderick J.J., 1998, *AJ*, 115, 1693
- Dickey J.M., Lockman F.J., 1990, *ARA&A*, 28, 215
- Dunn R.J.H., Fabian A.C., 2006, *MNRAS*, 373, 959
- Ebeling H., Mullis C.R., Tully R.B., 2002, *ApJ*, 580, 774
- Ebeling H., Ma C.J., Kneib J.-P., Jullo E., Courtney N.J.P., Barrett E., Edge A.C., Le Borgne J.-F., 2009, *MNRAS*, 395, 1213
- Eckert D., Produit N., Paltani S., Neronov A., Courvoisier T.J.L., 2008, *A&A*, 479, 27
- Edge A.C., Stewart G.C., Fabian A.C., Arnaud K.A., 1990, *MNRAS*, 245, 559
- Fabian A.C., Sanders J.S., Ettori S., Taylor G.B., Allen S.W., Crawford C.S., Iwasawa K., Johnstone R.M., 2001, *MNRAS*, 321, L33
- Fujita Y., Hayashida K., Nagai M., Inoue S., Matsumoto H., Okabe N., Reiprich T.H., Sarazin C.L., Takizawa M., 2008, *PASJ*, 60, 1133
- Hasegawa T., Wakamatsu K., Malkan M., Sekiguchi K., Menzies J.W., Parker Q.A., Jugaku J., Karoji H., Okamura S., 2000, *MNRAS*, 316, 326
- Harrison F.A. *et al.* 2005, *Experimental Astronomy*, 20, 131
- Govoni F., Murgia M., Markevitch M., Feretti L., Giovannini G., Taylor G.B., Carretti E., 2009, *A&A*, 499, 371
- Henry J.P., Finoguenov A., Briel U.G., 2004, *ApJ*, 615, 181
- Johnston M.D., Bradt H.V., Doxsey R.E., Marshall F.E., Schwartz D.A., Margon B., 1981, *ApJ*, 245, 799
- Kaastra J.S., Mewe R., 1993, *Legacy*, 3, 16
- Kalberla P.M., Burton W.B., Hartmann Dap, Arnal E.M., Bajaja E., Morras R., Poeppel W.G.L., 2005, *A&A*, 440, 775
- Landau L.D., Lifshitz E.M., 1959, *FluidMechanics, Course of Theoretical Physics Vol. 6*, Pergamon, Oxford
- Mahdavi A., Finoguenov A., Böhringer H., Geller M.J., Henry J.P., 2005, *ApJ*, 622, 187
- Mantz A., Allen S.W., Rapetti, D., Ebeling H., 2009a, submitted to *MNRAS*, astro-ph/0909.3098
- Mantz A., Allen S.W., Ebeling H., Rapetti D., Drlica-Wagner K.A., 2009b, submitted to *MNRAS*, astro-ph/0909.3099
- Markevitch M., Vikhlinin A., Mazzotta P., 2001, *ApJ*, 562L, 153
- Markevitch M., Vikhlinin A., 2007, *PhR*, 443, 1
- Matsuzawa H., Matsuoka M., Ikebe Y., Mihara T., Yamashita K., 1996, *PASJ*, 48, 565
- Million E.T., Allen S.W., 2009, *MNRAS*, 399, 1307
- Murgia M., Govoni F., Markevitch M., Feretti L., Giovannini G., Taylor G.B., Carretti E., 2009, *A&A*, 499, 679
- Nevalainen J., Oosterbroek T., Bonamente M., Colafrancesco S., 2004, *ApJ*, 608, 166
- Nevalainen J., Eckert D., Kaastra J., Bonamente M., Kettula K., 2009, *A&A*, in press, astro-ph/0910.1364
- Pérez-Torres M.A., Zandanel F., Guerrero M.A., Pal S., Profumo S., Prada F., Panessa F., 2009, *MNRAS*, 396, 2237
- Reiprich T.H., Sarazin C.L., Kempner J.C., Tittley E., 2001, *ApJ*, 608, 179
- Sanders, J.S., Fabian A.C., Dunn R.J.H., 2005, *MNRAS*, 360, 133
- Sanders J.S., 2006, *MNRAS*, 371, 829
- Sanders J.S., Fabian A.C., Taylor G.B., 2009, *MNRAS*, 393, 71
- Sun M., Jones C., Murray S.S., Allen S.W., Fabian A.C., Edge A.C., 2003, *ApJ*, 587, 619
- Sun M., Jones C., Forman W., Vikhlinin A., Donahue M., Voit M., 2007, *ApJ*, 657, 197
- Tittley E.R., Henrikson M., 2005, *ApJ*, 618, 227
- Vikhlinin A., Markevitch M., Murray S.S., 2001, *ApJ*, 551, 160
- Wakamatsu K., Malkan M.A., Nishida M.T., Parker Q.A., Saunders W., Watson F.G., 2005, in *ASP Conf. Ser. Vol. 329, Nearby Large-Scale Structures and the Zone of Avoidance*. Astron. Soc. Pac., San Francisco, p. 189
- Watanabe M., Yamashita K., Furuzawa A., Kunieda H., Tawara Y., 2001, *PASJ*, 53, 605
- Werner N., Durret F., Ohashi T., Schindler S., Wiersma R.P.C., 2008, *SSRv*, 134, 337